Research Article | Vol. 28, No. 13 / 22 June 2020 / Optics Express 19270
Optics EXPRESS

Photolithography allows high-Q AlN microresonators for near octave-spanning frequency comb and harmonic generation

JIA LIU,[1,3] HAIZHONG WENG,[2,3] ADNAN ALI AFRIDI,[2] JING LI,[2] JIANGNAN DAI,[1] XIANG MA,[1] HANLING LONG,[1] YI ZHANG,[1] QIAOYIN LU,[1] JOHN F. DONEGAN,[2,4] AND WEIHUA GUO[1,5]

[1]*Wuhan National Laboratory for Optoelectronics, and School of Optical and Electronic Information, Huazhong University of Science and Technology, 1037 Luoyu Road, Wuhan 430074, China*
[2]*School of Physics, CRANN and AMBER, Trinity College Dublin, Dublin 2, Ireland*
[3]*These authors contributed equally to this work and should be considered co-first authors.*
[4]*jdonegan@tcd.ie*
[5]*guow@mail.hust.edu.cn*

Abstract: Single-crystal aluminum nitride (AlN) possessing both strong Pockels and Kerr nonlinear optical effects as well as a very large band gap is a fascinating optical platform for integrated nonlinear optics. In this work, fully etched AlN-on-sapphire microresonators with a high-Q of 2.1×10^6 for the TE_{00} mode are firstly demonstrated with the standard photolithography technique. A near octave-spanning Kerr frequency comb ranging from 1100 to 2150 nm is generated at an on-chip power of 406 mW for the TM_{00} mode. Due to the high confinement, the TE_{10} mode also excites a Kerr comb from 1270 to 1850nm at 316 mW. In addition, frequency conversion to visible light is observed during the frequency comb generation. Our work will lead to a large-scale, low-cost, integrated nonlinear platform based on AlN.

1. Introduction

Integrated and miniaturized optical microresonators have a wide range of applications such as nonlinear optics, quantum electrodynamics, biochemical sensing and all-optical signal processing due to their small mode volume, high intra-cavity optical power density and strong interaction between the light field and the material [1–4]. Since the first demonstration in a silica microtoroid [5], the field of optical frequency comb (OFC) generated by cascaded four-wave mixing (FWM) in high-Q microcavities has made great progress and significantly impacted applications ranging from telecommunications and spectroscopy calibration to optical ranging and astronomy [6–9]. Various material platforms for OFC generation have been demonstrated, such as MgF_2 crystal cavities [10], high index silica glass (Hydex) [11], diamond [12] and silicon [13]. Silicon based materials such as silicon nitride [14–16] and silicon dioxide (SiO_2) [17,18] have attracted more attention due to the low propagation loss and mature manufacturing processes, in conjunction with the merits of CMOS compatibility and chip-scale integration. AlN featuring both strong Pockels (χ^2) and Kerr (χ^3) nonlinear effects [19] has been successfully used for second-harmonic generation (SHG) [20,21], third-harmonic generation (THG) [22] and electro-optic devices [23]. Especially the second-order nonlinearity can help broaden the spectrum of OFC into the visible regime, which is essential to achieve the key function of f-$2f$ (or $2f$-$3f$) self-referencing [24,25]. With a wide band gap (~6.0 eV), it shows optical transparency over a broad spectral range covering from the ultraviolet (UV) to the visible and infrared (IR) [26]. AlN is therefore a very versatile and useful platform for integrated nonlinear interactions, frequency conversion and self-referencing frequency combs.

#395013 https://doi.org/10.1364/OE.395013
Journal © 2020 Received 16 Apr 2020; revised 8 Jun 2020; accepted 9 Jun 2020; published 15 Jun 2020

Optics EXPRESS

Compared with AlN sputtered on silicon, wurtzite AlN epitaxially grown on sapphire exhibits superior crystalline quality and usually has higher optical Q [27,28]. For example, ultrahigh-Q UV microring resonators with potential applications in on-chip UV spectroscopy and nonlinear optics have been attained on a single-crystal AlN platform [29]. In the telecom C band, the first high-Q single-crystal AlN microresonator with an intrinsic Q (Q_{int}) of ~2.5 million was demonstrated by X. Liu, et al. [28], and the highest Q_{int} of ~2.8 million for microring resonators based on the 1-μm-thick single-crystal AlN film has been reported recently [30]. Considering its low loss and high nonlinearity (χ^2 and χ^3), a near octave-spanning Kerr comb (from 1075 to 2075nm) with 1 W on-chip power has been realized with a partially etched structure [31]. Mode-locked Kerr optical soliton generation was demonstrated [32]. A 17000%/W second-harmonic conversion efficiency in single-crystal AlN microresonators was obtained [21].

To date, lithography and etching challenges have made it very difficult to achieve fully etched devices with thick (>1.2 μm) AlN-on-sapphire films due to the strength of the Al-N bonds. Deep ultraviolet (DUV) lithography has been successfully implemented to fabricate high-Q microresonators and realized the ultra-low threshold OFC generation based on some material platforms, such as S_3iN_4, AlGaAs, etc. [33–35]. AlN microresonator fabrication, however, rarely utilizes simple photolithography instead using electron beam lithography (EBL), although the former method will be essential for manufacturing large-scale integrated devices. In this work, for the first time, standard photolithography and inductively coupled plasma (ICP) etching are used to fully etch 1.2-μm-thick AlN-on-sapphire films, which allows easy integration of microcavities with other optical elements. By optimizing the fabrication process, a high Q_{int} of 2.1×10^6 is obtained for the transverse-electric fundamental (TE_{00}) mode. The corresponding propagation loss is estimated to be 0.17 dB/cm, which is comparable to the results of devices fabricated with EBL. Due to the enhanced confinement for modes, a broadband Kerr frequency comb ranging from 1100 to 2150 nm is generated by pumping the transverse-magnetic fundamental (TM_{00}) mode around 1560 nm at 406 mW power. Red and green emissions are also observed with a visible CCD camera due to the harmonic generation and sum frequency generation.

2. Fabrication and measurement

The single-crystal AlN film is grown on a sapphire substrate (0001) by metal organic chemical vapor deposition (MOCVD) using the process reported in Ref. [36]. A 1.2-μm-thick AlN film is selected to reduce the scattering loss caused by lattice mismatch at the interface between AlN and sapphire, while ensuring the control of geometric dispersion. A schematic illustration of the fabrication process is shown in Fig. 1. After depositing an 800-nm-thick SiO_2 hard mask by plasma enhanced chemical vapor deposition (PECVD), a 70-nm-thick chromium (Cr) is further deposited, prior to the photoresist spinning, as a metal mask to etch SiO_2 due to the low etching selectivity between SiO_2 and photoresist. A 900-nm-thick SPR955-0.9 photoresist is spin coated onto the film without bottom anti-reflective coatings. The ring resonators and bus waveguides are defined using a purchased stepper reticle and the Nikon NSR-2005i9C Stepper System based on i-line UV illumination (365 nm Hg spectral peak). Then, a post-exposure bake is used to cure the surface roughness of the photoresist pattern. Next, the pattern is transferred to the Cr mask and SiO_2 hard mask sequentially by ICP-RIE using Cl_2/O_2 and SF_6/Ar, respectively. After removing the Cr mask, the SiO_2 mask is used to etch the AlN layer completely with an optimized $Cl_2/BCl_3/Ar$-based ICP-RIE dry etching process. Finally, devices are encapsulated in 1.5-μm-thick PECVD-SiO_2 and cleaved prior to the measurement. No additional annealing is performed throughout the fabrication process. This process provides a new route for AlN-on-sapphire fabrication, requiring photolithography instead of EBL as in previous reports. The etching rate of AlN is about 205 nm/min, which is slightly lower than the reported previously [28]. In addition, a 1.4-μm-thick SiO_2 mask can be etched completely due to the thicker SPR photoresist and the high etching selectivity between SiO_2 and Cr. With a

Optics EXPRESS

selectivity of 2.4:1 between AlN and SiO_2, a 3.1-μm-thick AlN is allowed to be fully etched, which is thicker than 1.4 μm estimated previously [21].

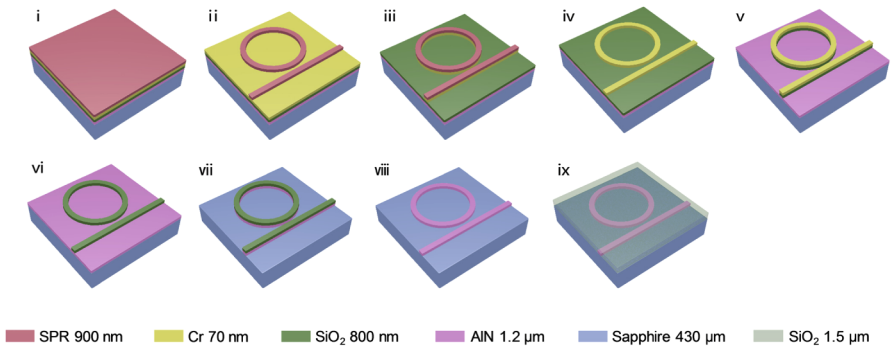

Fig. 1. Schematic illustration of the fabrication process for the AlN-on-sapphire microresonator.

A chip with a set of ~360 GHz free-spectral-range (FSR) microresonators (ring radius of 60 μm) is fabricated. For OFC generation, the crucial question is the maximum achievable bandwidth which is strongly limited by the mismatch between equidistant comb modes and the non-equidistant resonator modes which caused by the dispersion in the cold cavity [37]. When high light intensities are circulating within cavity, the cross-phase and self-phase modulation arising from the Kerr effect will potentially make the resonator modes equidistant. It always leads to a resonance redshift at higher power and consequently it is only possible to compensate an appropriately anomalous group velocity dispersion (GVD). Typically, the evolution of Kerr frequency combs is governed by the mean-field Lugiato-Lefever equation and indicates that a small GVD and a large nonlinearity are indispensable to access broadband Kerr comb [38]. Due to the normal dispersion found in bulk AlN material, we need to adjust the geometric size of the ring resonator to acquire an overall anomalous dispersion.

The GVD profiles of the microring resonators are calculated theoretically using a finite-element method (FEM) solver. Here, we have considered the experimental structure with the radius of 60 μm and 75° sidewall slope angle induced by dry etching of AlN. Figure 2 compares the simulated dispersion of different modes in the resonators with widths of 1.8, 2.6 and 3.6 μm. We can learn that the anomalous dispersion increases with the decrease of the ring width for both TM and TE fundamental modes. The large and near-zero anomalous-GVD bandwidth spanning an octave is achievable for the TM_{00} mode when the width is 3.6 μm. For the TE_{00} mode, a 2.6-μm width is more suitable as 3.6 μm presents normal dispersion when the operating wavelength lower than 1700nm and 1.8 μm has a rather large anomalous dispersion. For the higher-order modes, due to the strong interaction with the geometric boundary caused by the larger mode spot, they are often accompanied by a higher anomalous dispersion than the fundamental mode. We can find that when the width is 3.6 μm, the TE_{10} mode shows anomalous dispersion above 1300 nm and is considered to have the potential to directly generate Kerr frequency comb by cascaded FWM as found in subsequent studies.

The microscope and scanning electron microscopy (SEM) images of the fabricated AlN microresonators are shown in Fig. 3. All microring resonators are side coupled to the straight waveguides of different widths with varying gaps. The waveguides from the coupling region to both ends are tapered increasing from ~0.91 to 4 μm to improve the fiber coupling efficiency and are offset 10° from horizontal to prevent reflection, as shown in Fig. 3(a). Figure 3(b) shows the coupling area between the microring and the bus waveguide after AlN etching. Clearly, the 0.5 μm gap was defined very well by the photolithography and ICP dry etching. The fully etched

Optics EXPRESS

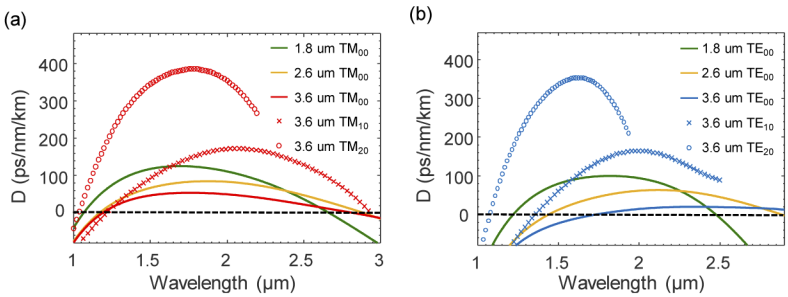

Fig. 2. Simulation provides GVD of (a) TM modes and (b) TE modes for 1.8, 2.6 and 3.6-μm-wide microring resonators.

cross section of rings with 75° sidewall slope angle induced by dry etching of AlN is illustrated in Fig. 3(c). Figure 3(d) shows a smooth sidewall of the microresonator after etching. In the following, we will present and discuss the measurement results for the microresonator with 1.2 × 3.6 μm^2 cross section, 60 μm radius and the bus waveguide with 0.91 μm width, while the gap between them is 0.5 μm.

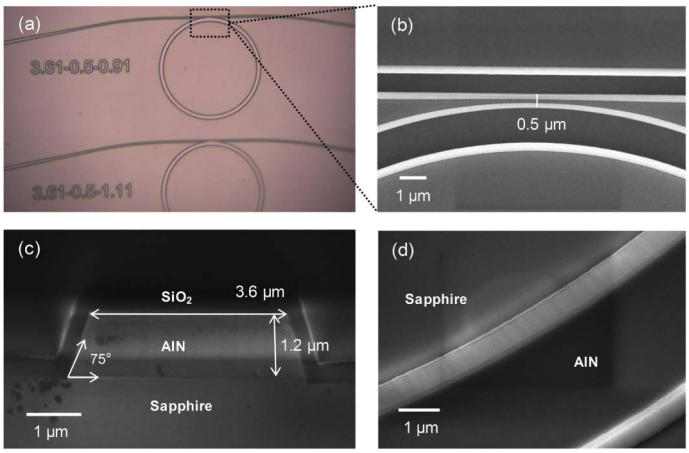

Fig. 3. (a) Microscope image of the fabricated devices. SEM images for (b) top-view of enlarged coupling regime, (c) side-view of the cleaved ring resonator and (d) top-view of enlarged resonator, showing a smooth sidewall.

The performance of the microresonators are measured using a Santec TSL-710 tunable laser (linewidth < 100 kHz) with -10 dBm output power. By recording the output power with a Santec power monitor (MPM210) synched with the tunable laser, we can obtain the transmission spectrum with 0.1 pm resolution. Figure 4(a) shows the transmission spectra for the TM and TE modes. The microresonator exhibits various resonance modes when excited with different polarized light which is controlled by a fiber polarization controller (FPC). As shown in Fig. 4(a), the total chip insertion loss is about 8 dB (4 dB/facet) for both polarization states. Among them, the FSRs of TM_{00}, TE_{00} and TE_{10} modes around 1560 nm are about 363.4, 375.2 and 376.2 GHz, which are consistent with the simulation results 364.3, 375.3 and 376.5 GHz. Figures 4(b) and 4(c) show the Lorentz fitting curves for the TM_{00} and TE_{10} mode at 1559.47 and 1559.75 nm, respectively. According to the fitted full width half maximum (FWHM), the loaded Q (Q_{load}) of the two modes are calculated to be 6.1 × 10^5 and 6.2 × 10^5. The Q_{int} can be estimated as 1.5 × 10^6 and 1.2 × 10^6, corresponding to the loss of 0.26 and 0.3 dB/cm, respectively. Figure 4(d)

Optics EXPRESS

shows a resonance splitting for TE_{00} mode due to the coherent backscattering of light from fabrication imperfections or surface roughness [30]. The estimated Q_{int} based on the measured resonance spectra is 2.1×10^6, corresponding to the loss of 0.17 dB/cm. Higher-order modes also can be strongly confined with low transmission loss, which is attractive for achieving phase matching in frequency conversion and enhancing the utilization of microresonators. Extinction ratios for the modes can reach as high as 17 dB. Therefore, the simple photolithography and dry etching process enable a high-Q microresonator with a gap of only 500 nm which is close to critical coupling for all TE and TM modes. Critical coupling improves the intracavity power buildup and reduces the pump power required for nonlinear optical processes.

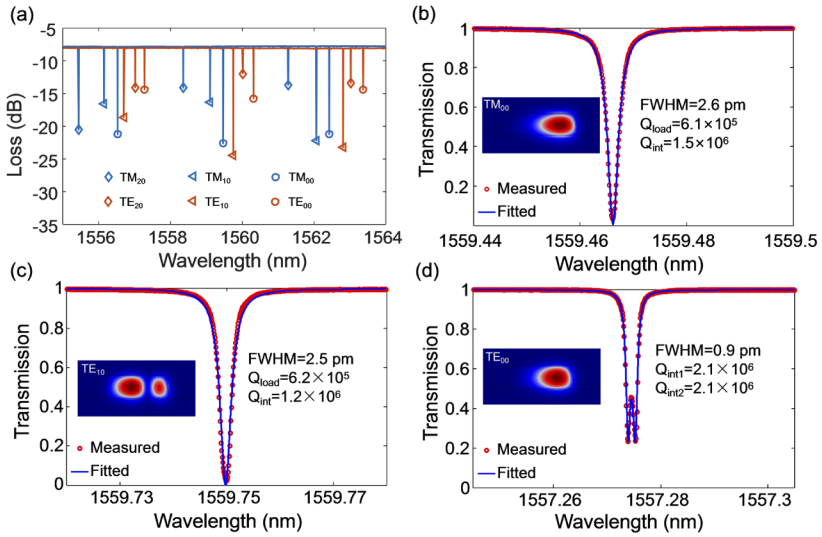

Fig. 4. (a) Spectra of the resonance near 1560 nm, where three sets of modes fundamental, first-order and second-order for different polarizations are marked with circle, triangle, and square symbols, respectively. Zoom views of (b) TM_{00} and (c) TE_{10} mode resonance spectrum and the Lorentzian fitting. (d) Zoom view of TE_{00} mode resonance spectra, wherein the resonance shows doublet splitting due to coherent backscattering. The insets show simulated electrical field distributions in the cross section of the ring.

3. Frequency comb generation

The experimental set-up for Kerr comb generation is illustrated in Fig. 5(a). CW light is amplified by an erbium-doped fiber amplifier (EDFA) and launched into the microresonator through the bus waveguide. The OFC can be initiated by tuning the pump wavelength into resonance. For TM_{00} mode at 1559.47 nm, by setting the pump (on-chip) power at 270 mW, we tune the pump wavelength gradually from blue shifted to red shifted and plot the comb spectrum. The threshold power is measured to be around 50 mW. In addition, based on the nonlinear index $n_2 = 3.5 \times 10^{-19}$ $m^2 \cdot W^{-1}$ reported in [31], the threshold power can also be calculated by the formula:

$$P_{th} \approx 1.54 \frac{\pi}{2} \left(\frac{Q_c}{2Q_{load}} \right) \frac{n^2 V_{eff}}{n_2 \lambda {Q_{load}}^2} \tag{1}$$

where n (~2.1 around 1560 nm) is the refractive index of AlN and V_{eff} is the effective mode volume calculated with FEM at the pump wavelength. Taking into account the coupling Q ($Q_c = 1.1 \times 10^6$) from the measured result, the threshold of the TM_{00} mode is determined to be 44 mW. Figure 5(b) indicates that the evolution (from state i-vi) accords with the scenario

Optics EXPRESS

of multiple-mode-spaced (MMS) combs [39]. For instance, the first parametric sidebands of TM_{00} mode are generated at a spacing of multiple FSRs and referred to as primary comb lines. The primary comb lines are preserved as pump lines to generate subcombs via degenerate or non-degenerate FWM processes at later stages of the comb evolution. When the power coupled to the cavity is increased further, the subcombs merge and lead to spectral lines with a shape similar to parametric gain lobes. The new lines may also appear between two previously existing strong lines by non-degenerate processes. Eventually, broadband Kerr combs are observed yielding single-FSR-spaced lines. The RF beat note accompanying the formation of the OFC is recorded in Fig. 5(c) using an electrical spectrum analyzer (ESA). The broad RF beat note observed in this system indicates the formation of a high-noise OFC and verifies the generation of MMS combs. Although this comb state therefore exhibits low coherence and is unsuitable for metrology, the transition to low noise has been proven to exist and implemented in many material platforms [39,40]. For the TE_{00} mode, the formation of Kerr OFC was not observed. The broadband Kerr OFC is obtained through TE_{10} mode and the evolution process is similar to the TM_{00} mode. This is consistent with the GVD simulation results above.

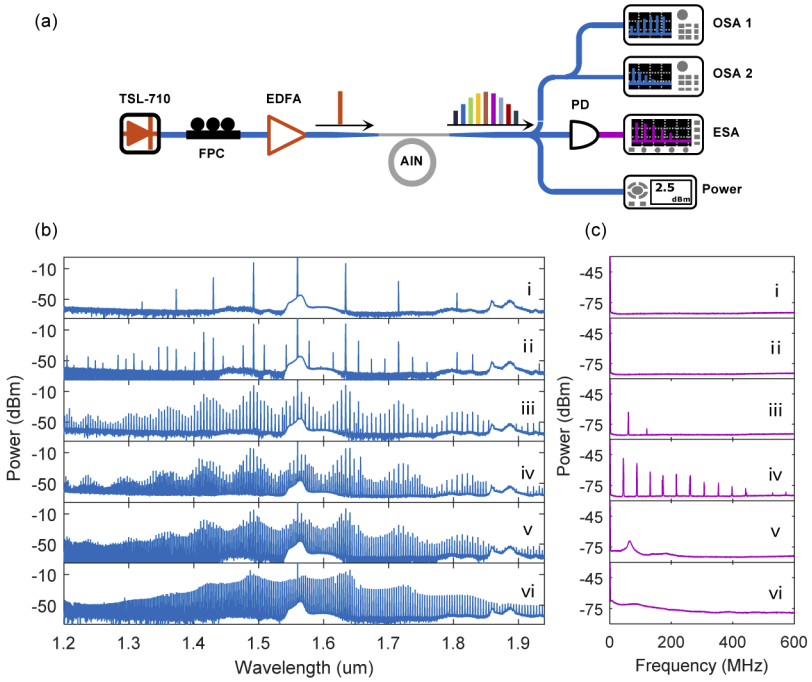

Fig. 5. (a) Schematic of the setup used to generate Kerr combs using the Santec TSL-710 tunable laser (FPC: fiber polarization controller, EDFA: erbium-doped fiber amplifier, PD: photodetector, OSA: optical spectrum analyzer, ESA: electrical spectrum analyzer). (b) Evolution of the optical frequency comb spectrum for the TM_{00} mode with pump power of 270 mW. (c) RF beat note generated in the resonator while tuning the pump wavelength into resonance.

The resonance frequencies of a microresonator can be Taylor-expanded around a central pump frequency ω_0, using the relative mode numbers $\mu_r = \mu - \mu_0$:

$$\omega_{\mu_r} = \omega_0 + D_1 \cdot \mu_r + \frac{D_2}{2!} \cdot {\mu_r}^2 + \frac{D_3}{3!} \cdot {\mu_r}^3 + \ldots \tag{2}$$

where $D_1/2\pi$ is the FSR of the resonator and $D_2/2\pi$ is the difference of the two FSRs adjacent to the pump frequency ω_0 and linked to the GVD. The integrated dispersion D_{int} is introduced to

Optics EXPRESS

describe the deviation of a given resonance from an equidistant frequency grid defined by the FSR around the central pump frequency:

$$D_{\mathrm{int}}(\mu_r) = \omega_{\mu_r} - (\omega_0 + D_1 \cdot \mu_r) \tag{3}$$

For a microresonator with anomalous GVD ($D_2 > 0$), the third-order nonlinearity leads to a nonlinear phase shift that can compensate for the resonant frequency deviation to reach a certain spectral bandwidth. Beyond this, the power of the microcomb lines in the spectral endpoints can be enhanced where the linear phase-matching condition $D_{\mathrm{int}}(\mu_r) = 0$ is satisfied, and such a dispersive wave-like (DW-like) bump offers an effective way to extend the comb spectra into the normal GVD regime [41]. Figure 6 shows the simulated D_{int} for the TM_{00} and TE_{10} modes with the red curves, where the $D_2/2\pi$ is 7.3 and 14 MHz at the pump wavelength, respectively. For the TM_{00} mode at 1559.47 nm, when the on-chip power is increased to 406 mW, a broadband comb spectrum ranging from 1100 to 2150 nm is realized, recorded by two optical spectrum analyzers (OSAs) covering different wavelength ranges. A DW-like bump is observed around 1180 nm for the comb spectrum, which agrees well with the simulation result. For the TE_{10} mode at 1559.75 nm, the excited comb ranges from 1270 to 1850nm when the power is 316 mW, where the DW-like bump is observed around 1300 nm. Therefore, the fully etched AlN microring resonator not only achieves nearly octave-spanning OFC at low power, but also, for the high-order TE_{10} mode, directly realizes OFC produced by FWM.

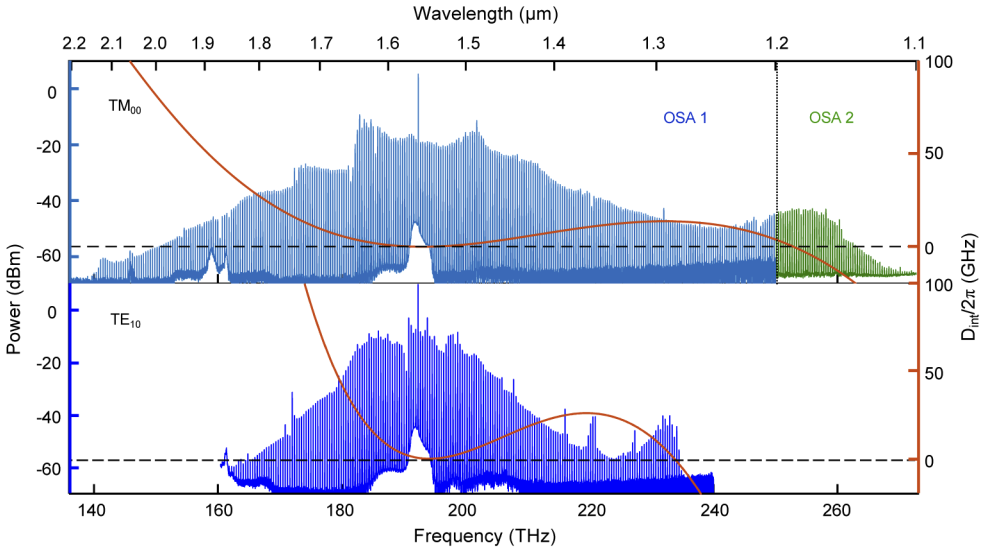

Fig. 6. Comb spectrum generated from 1100 to 2150 nm at the on-chip power of 406 mW for the TM_{00} mode (upper) and from 1270 to 1850nm with 316 mW for the TE_{10} mode (lower). The red curve is the simulation of the D_{int}.

Considering that Si_3N_4 is heavily researched and has a linear and nonlinear refractive index similar to AlN, we compare the performance of AlN and Si_3N_4 integrated microresonators reported previously and summarize in Table 1. Si_3N_4 microresonators have reached Q factor more than 10 million and realized the octave-spanning soliton [42,43]. Here, an optical comb spectral ranging close to 1050 nm is achieved, which is the widest Kerr comb for reported AlN microresonators while the power is much lower. Even though our results are outstanding in current AlN microresonators, the Q factors still need to be improved further to reach the value for the Si_3N_4 resonators. More importantly, the fabrication using standard photolithography is

Optics EXPRESS

proven to be feasible and will create more attractive applications in the large-scale manufacturing of low-loss and high-power nonlinear devices.

Table 1. Performance comparison of Kerr combs based on AlN and Si_3N_4 integrated microresonators

Material	Pattern definition	FSR (GHz)	Cross-section height × width (μm^2)	Q_{int}	Power (mW)	Spanning (nm)
Si_3N_4 [15]	EBL	226	0.725×1.65	3×10^6	400	1170-2350
Si_3N_4 [42]	EBL	24.7	0.6×3.0	1.7×10^7	24	1510-1600
Si_3N_4 [43]	EBL	1000	0.6×1.76	1×10^6	40	1050-2100[a]
Si_3N_4 [44]	EBL	194	0.73×1.8	8×10^6	2.5	1520-1640[a]
Si_3N_4 [45]	EBL	100	0.74×2.0	1.25×10^7	100	1460-1700[a]
Si_3N_4 [46]	Photolithography	9.8	0.95×2.1	2.3×10^7	56	1520-1600[a]
Polycrystalline AlN [27]	EBL	370	0.65×3.5	0.88×10^6	500	1420-1670
Single-crystal AlN [31]	EBL	369	1.2×3.5	1.6×10^6	1000	1075-2075
Our work AlN	**Photolithography**	**363**	**1.2×3.6**	$\mathbf{1.5\times10^6}$	**406**	**1100-2150**

[a]Represents the generation of optical solitons.

4. Harmonic generation

The Kerr comb from FWM is not the only nonlinear phenomenon observed from the AlN material system. Usually, it is difficult to produce OFCs at short wavelength due to normal dispersion of the material. Fortunately, AlN features strong χ^2 and χ^3 nonlinearities, so other nonlinear effects such as SHG and THG can be generated to get the frequency lines from green light to the IR region [20,22,47]. Deeply etched waveguides certainly reduce the volume of modes and enhance nonlinear optical interaction. In addition, as mentioned above, the low transmission loss of high-order modes makes it possible to confine the phase-matched higher-order visible modes within the ring resonators. Therefore, resonant enhanced wave-mixing in microcavities are leveraged to generate new frequency lines in the red and green regions.

For efficient wavelength conversion, the phase matching condition should be satisfied. For fully etched microring resonators, confinement of both the fundamental and higher-order modes mean that there are more opportunities for achieving phase matching during frequency conversion. The wavelength conversion for TM_{00} mode from IR to visible wavelength is monitored by a visible CCD camera. Figures 7(a) and 7(b) show the red and green emission from the ring resonator under different states of OFC generation, which may mean that SHG, THG or sum frequency

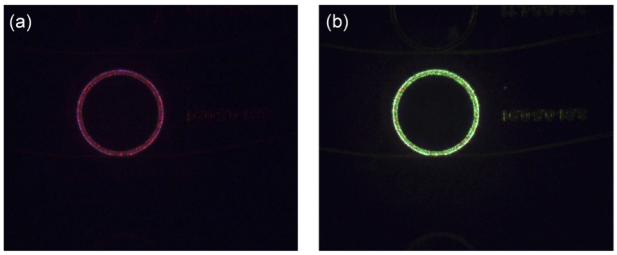

Fig. 7. (a) Red and (b) green light images collected by the CCD camera under conditions of strong comb formation.

Optics EXPRESS

generation are all occurring. The visible emission in the form of combs in the red and green region needs further exploration.

5. Summary

For the first time, simple photolithography and ICP dry etching process are applied to fully etched microresonators based on a 1.2-μm-thick AlN film. A 0.5 μm gap can be achieved to realize nearly critical coupling for TM and TE modes. By optimizing the dry etching condition, a high Q_{int} of 1.5×10^6 for TM_{00} mode is obtained and a near octave-spanning Kerr comb is generated from 1100 to 2150 nm at an on-chip power of 406 mW. A high Q_{int} of 2.1×10^6 is also obtained for the TE_{00} mode. Thanks to the full etching, the TE_{10} mode also has a high Q_{int} of 1.2×10^6 and is used to generate OFC spanning from 1270 to 1850 nm at 316 mW. These prove that the performance of the device manufactured by this process is comparable to the results of EBL. With a strong χ^2 and χ^3 optical nonlinearity, in conjunction with more confinement of high-order modes, frequency conversion to visible light is observed. Based on the superior performance, octave-spanning Kerr soliton combs should be developed for this platform in the near future. Photolithography will make a strong impact on the development and application of comb-based microresonators due to its simplicity guaranteeing a high yield of devices.

Funding

National Natural Science Foundation of China (61861136001); Science Foundation Ireland (17/NSFC/4918).

Disclosures

The authors declare no conflicts of interest.

References

1. A. A. Savchenkov, A. B. Matsko, D. Strekalov, M. Mohageg, V. S. Ilchenko, and L. Maleki, "Low threshold optical oscillations in a whispering gallery mode CaF_2 resonator," Phys. Rev. Lett. **93**(24), 243905 (2004).
2. S. M. Spillane, T. J. Kippenberg, K. J. Vahala, K. W. Goh, E. Wilcut, and H. J. Kimble, "Ultrahigh-Q toroidal microresonators for cavity quantum electrodynamics," Phys. Rev. A **71**(1), 013817 (2005).
3. A. M. Armani, R. P. Kulkarni, S. E. Fraser, R. C. Flagan, and K. J. Vahala, "Label free, single-molecule detection with optical microcavities," Science **317**(5839), 783–787 (2007).
4. C. Koos, P. Vorreau, T. Vallaitis, P. Dumon, and W. Bogaerts, "All-optical high-speed signal processing with silicon-organic hybrid slot waveguides," Nat. Photonics **3**(4), 216–219 (2009).
5. P. Del'Haye, A. Schliesser, O. Arcizet, T. Wilken, R. Holzwarth, and T. J. Kippenberg, "Optical frequency comb generation from a monolithic microresonator," Nature **450**(7173), 1214–1217 (2007).
6. J. Pfeifle, V. Brasch, M. Lauermann, Y. Yu, D. Wegner, T. Herr, and R. Schmogrow, "Coherent terabit communications with microresonator Kerr frequency combs," Nat. Photonics **8**(5), 375–380 (2014).
7. M.-G. Suh, Q.-F. Yang, K. Y. Yang, X. Yi, and K. J. Vahala, "Microresonator soliton dual-comb spectroscopy," Science **354**(6312), 600–603 (2016).
8. P. Trocha, M. Karpov, D. Ganin, M. H. P. Pfeiffer, A. Kordts, S. Wolf, J. Krockenberger, P. M. Palomo, C. Weimann, S. Randel, W. Freude, T. J. Kippenberg, and C. Koos, "Ultrafast optical ranging using microresonator soliton frequency combs," Science **359**(6378), 887–891 (2018).
9. E. Obrzud, M. Rainer, A. Harutyunyan, M. H. Anderson, J. Liu, M. Geiselmann, B. Chazelas, S. Kundermann, S. Lecomte, M. Cecconi, A. Ghedina, E. Molinari, F. Pepe, F. Wildi, F. Bouchy, T. J. Kippenberg, and T. Herr, "A microphotonic astrocomb," Nat. Photonics **13**(1), 31–35 (2019).
10. W. Liang, A. A. Savchenkov, A. B. Matsko, V. S. Ilchenko, D. Seidel, and L. Maleki, "Generation of near-infrared frequency combs from a MgF_2 whispering gallery mode resonator," Opt. Lett. **36**(12), 2290–2292 (2011).
11. D. J. Moss, R. Morandotti, A. L. Gaeta, and M. Lipson, "New CMOS-compatible platforms based on silicon nitride and Hydex for nonlinear optics," Nat. Photonics **7**(8), 597–607 (2013).
12. B. J. M. Hausmann, I. Bulu, V. Venkataraman, P. Deotare, and M. Loncar, "Diamond nonlinear photonics," Nat. Photonics **8**(5), 369–374 (2014).
13. A. G. Griffith, R. K. W. Lau, J. Cardenas, Y. Okawachi, A. Mohanty, R. Fain, and A. L. Gaeta, "Silicon-chip mid-infrared frequency comb generation," Nat. Commun. **6**(1), 6299 (2015).

Optics EXPRESS

14. J. S. Levy, A. Gondarenko, M. A. Foster, A. C. Turner-Foster, A. L. Gaeta, and M. Lipson, "CMOS-compatible multiple-wavelength oscillator for on-chip optical interconnects," Nat. Photonics **4**(1), 37–40 (2010).
15. Y. Okawachi, K. Saha, J. S. Levy, Y. H. Wen, M. Lipson, and A. L. Gaeta, "Octave-spanning frequency comb generation in a silicon nitride chip," Opt. Lett. **36**(17), 3398–3400 (2011).
16. Y. Liu, Y. Xuan, X. Xue, P.-H. Wang, S. Chen, A. J. Metcalf, J. Wang, D. E. Leaird, M. Qi, and A. M. Weiner, "Investigation of mode coupling in normal-dispersion silicon nitride microresonators for Kerr frequency comb generation," Optica **1**(3), 137–144 (2014).
17. T. J. Kippenberg, R. Holzwarth, and S. A. Diddams, "Microresonator-based optical frequency combs," Science **332**(6029), 555–559 (2011).
18. P. Del'Haye, T. Herr, E. Gavartin, M. L. Gorodetsky, R. Holzwarth, and T. J. Kippenberg, "Octave spanning tunable frequency comb from a microresonator," Phys. Rev. Lett. **107**(6), 063901 (2011).
19. H. Jung, K. Y. Fong, C. Xiong, and H. X. Tang, "Electrical tuning and switching of an optical frequency comb generated in aluminum nitride microring resonators," Opt. Lett. **39**(1), 84–87 (2014).
20. X. Guo, C. L. Zou, and H. X. Tang, "Second-harmonic generation in aluminum nitride microrings with 2500%/W conversion efficiency," Optica **3**(10), 1126–1131 (2016).
21. A. W. Bruch, X. Liu, X. Guo, J. B. Surya, Z. Gong, L. Zhang, and H. X. Tang, "17000%/W second-harmonic conversion efficiency in single-crystalline aluminum nitride microresonators," Appl. Phys. Lett. **113**(13), 131102 (2018).
22. H. Jung, R. Stoll, X. Guo, D. Fischer, and H. X. Tang, "Green, red, and IR frequency comb line generation from single IR pump in AlN microring resonator," Optica **1**(6), 396–399 (2014).
23. C. Xiong, W. H. P. Pernice, and H. X. Tang, "Low-loss, silicon integrated, aluminum nitride photonic circuits and their use for electro-optic signal processing," Nano Lett. **12**(7), 3562–3568 (2012).
24. J. D. Jost, E. Lucas, T. Herr, C. Lecaplain, V. Brasch, M. H. P. Pfeiffer, and T. J. Kippenberg, "All-optical stabilization of a soliton frequency comb in a crystalline microresonator," Opt. Lett. **40**(20), 4723–4726 (2015).
25. J. D. Jost, T. Herr, C. Lecaplain, V. Brasch, M. H. Pfeiffer, and T. J. Kippenberg, "Counting the cycles of light using a self-referenced optical microresonator," Optica **2**(8), 706–711 (2015).
26. J. Li, K. B. Nam, M. L. Nakarmi, J. Y. Lin, H. X. Jiang, P. Carrier, and S.-H. Wei, "Band structure and fundamental optical transitions in wurtzite AlN," Appl. Phys. Lett. **83**(25), 5163–5165 (2003).
27. H. Jung and H. X. Tang, "Aluminum nitride as nonlinear optical material for on-chip frequency comb generation and frequency conversion," Nanophotonics **5**(2), 263–271 (2016).
28. X. Liu, C. Sun, B. Xiong, L. Wang, J. Wang, Y. Han, Z. Hao, H. Li, Y. Luo, J. Yan, T. Wei, Y. Zhang, and J. Wang, "Aluminum nitride-on-sapphire platform for integrated high-Q microresonators," Opt. Express **25**(2), 587–594 (2017).
29. X. Liu, A. W. Bruch, Z. Gong, J. Lu, J. B. Surya, L. Zhang, and H. X. Tang, "Ultra-high-Q UV microring resonators based on a single-crystalline AlN platform," Optica **5**(10), 1279–1282 (2018).
30. Y. Sun, W. Shin, D. A. Laleyan, P. Wang, A. Pandey, X. Liu, and Z. Mi, "Ultrahigh Q microring resonators using a single-crystal aluminum-nitride-on-sapphire platform," Opt. Lett. **44**(23), 5679–5682 (2019).
31. X. Liu, C. Sun, B. Xiong, L. Wang, J. Wang, Y. Han, Z. Hao, H. Li, Y. Luo, J. Yan, T. Wei, Y. Zhang, and J. Wang, "Integrated High-Q Crystalline AlN Microresonators for Broadband Kerr and Raman Frequency Combs," ACS Photonics **5**(5), 1943–1950 (2018).
32. Z. Gong, A. Bruch, M. Shen, X. Guo, H. Jung, L. Fan, and J. Yan, "High-fidelity cavity soliton generation in crystalline AlN micro-ring resonators," Opt. Lett. **43**(18), 4366–4369 (2018).
33. J. Liu, A. S. Raja, M. Karpov, B. Ghadiani, M. H. P. Pfeiffer, B. Du, N. J. Engelsen, H. Guo, Mi. Zervas, and T. J. Kippenberg, "Ultralow-power chip-based soliton microcombs for photonic integration," Optica **5**(10), 1347–1353 (2018).
34. S. P. Yu, T. C. Briles, G. T. Moille, X. Lu, S. A. Diddams, K. Srinivasan, and S. B. Papp, "Tuning Kerr-soliton frequency combs to atomic resonances," Phys. Rev. Appl. **11**(4), 044017 (2019).
35. L. Chang, W. Xie, H. Shu, Q.-F. Yang, B. Shen, A. Boes, J. D. Peters, W. Jin, C. Xiang, S. Liu, G. Moille, S.-P. Yu, X. Wang, K. Srinivasan, S. B. Papp, K. Vahala, and J. E. Bowers, "Ultra-efficient frequency comb generation in AlGaAs-on-insulator microresonators," Nat. Commun. **11**(1), 1331 (2020).
36. Y. Zhang, H. Long, J. Zhang, B. Tan, Q. Chen, S. Zhang, and C. Chen, "Fast growth of high quality AlN films on sapphire using a dislocation filtering layer for ultraviolet light-emitting diodes," CrystEngComm **21**(27), 4072–4078 (2019).
37. T. J. Kippenberg, S. M. Spillane, and K. J. Vahala, "Kerr-nonlinearity optical parametric oscillation in an ultrahigh-Q toroid microcavity," Phys. Rev. Lett. **93**(8), 083904 (2004).
38. S. Coen, H. G. Randle, T. Sylvestre, and M. Erkintalo, "Modeling of octave-spanning Kerr frequency combs using a generalized mean-field Lugiato-Lefever model," Opt. Lett. **38**(1), 37–39 (2013).
39. T. Herr, K. Hartinger, J. Riemensberger, C. Y. Wang, E. Gavartin, R. Holzwarth, and T. J. Kippenberg, "Universal formation dynamics and noise of Kerr-frequency combs in microresonators," Nat. Photonics **6**(7), 480–487 (2012).
40. J. Li, H. Lee, T. Chen, and K. J. Vahala, "Low-pump-power, low-phase-noise, and microwave to millimeter-wave repetition rate operation in microcombs," Phys. Rev. Lett. **109**(23), 233901 (2012).
41. M. H. Pfeiffer, C. Herkommer, J. Liu, H. Guo, M. Karpov, E. Lucas, and T. J. Kippenberg, "Octave-spanning dissipative Kerr soliton frequency combs in Si_3N_4 microresonators," Optica **4**(7), 684–691 (2017).

Optics EXPRESS

42. Y. Xuan, Y. Liu, L. T. Varghese, A. J. Metcalf, X. Xue, P. H. Wang, and S. Kim, "High-Q silicon nitride microresonators exhibiting low-power frequency comb initiation," Optica **3**(11), 1171–1180 (2016).
43. Q. Li, T. C. Briles, D. A. Westly, T. E. Drake, J. R. Stone, B. R. Ilic, S. A. Diddams, S. B. Papp, and K. Srinivasan, "Stably accessing octave-spanning microresonator frequency combs in the soliton regime," Optica **4**(2), 193–203 (2017).
44. B. Stern, X. Ji, Y. Okawachi, A. L. Gaeta, and M. Lipson, "Battery-operated integrated frequency comb generator," Nature **562**(7727), 401–405 (2018).
45. Z. Ye, K. Twayana, P. A. Andrekson, and V. Torres-Company, "High-Q Si_3N_4 microresonators based on a subtractive processing for Kerr nonlinear optics," Opt. Express **27**(24), 35719–35727 (2019).
46. J. Liu, E. Lucas, A. S. Raja, J. He, J. Riemensberger, R. N. Wang, M. Karpov, H. Guo, R. Bouchand, and T. J. Kippenberg, "Photonic microwave generation in the X- and K-band using integrated soliton microcombs," *Nat. Photonics* (2020).
47. X. Liu, C. Sun, B. Xiong, L. Wang, J. Wang, Y. Han, Z. Hao, H. Li, Y. Luo, J. Yan, T. Wei, Y. Zhang, and J. Wang, "Generation of multiple near-visible comb lines in an AlN microring via $\chi^{(2)}$ and $\chi^{(3)}$ optical nonlinearities," Appl. Phys. Lett. **113**(17), 171106 (2018).